metals

MDPI

Article

Influence of Surface Mechanical Attrition Treatment (SMAT) on Microstructure, Tensile and Low-Cycle Fatigue Behavior of Additively Manufactured Stainless Steel 316L

Thomas Wegener [1,*,†], Tao Wu [1,2,3,*,†], Fei Sun [4], Chong Wang [5], Jian Lu [6] and Thomas Niendorf [1]

[1] Institut für Werkstofftechnik, Metallische Werkstoffe, Universität Kassel, Mönchebergstraße 3, 34125 Kassel, Germany
[2] Research Center Carbon Fibers Saxony (RCCF), Technische Universität Dresden, Breitscheidstraße 78, 01237 Dresden, Germany
[3] Fraunhofer Institute for Ceramic Technologies and Systems (IKTS), Winterbergstraße 28, 01277 Dresden, Germany
[4] Department of Materials Design Innovation Engineering, Graduate School of Engineering, Nagoya University, Furo-cho, Chikusa-ku, Nagoya 464-8603, Japan
[5] Institute of Solid Mechanics, Beihang University, 37 Xueyuan Road, Beijing 100083, China
[6] Department of Mechanical Engineering, City University of Hong Kong, 83 Tat Chee Ave, Hongkong 518057, China
* Correspondence: t.wegener@uni-kassel.de (T.W.); tao.wu1@mailbox.tu-dresden.de (T.W.)
† These authors contributed equally to this work.

Abstract: Direct Energy Deposition (DED), as one common type of additive manufacturing, is capable of fabricating metallic components close to net-shape with complex geometry. Surface mechanical attrition treatment (SMAT) is an advanced surface treatment technology which is able to yield a nanostructured surface layer characterized by compressive residual stresses and work hardening, thereby improving the fatigue performances of metallic specimens. In the present study, stainless steel 316L specimens were fabricated by DED and subsequently surface treated by SMAT. Both uniaxial tensile tests and uniaxial tension-compression low-cycle fatigue tests were conducted for as-built and SMAT processed specimens. The microstructure of both conditions was characterized by roughness and hardness measurements, scanning electron microscopy and transmission electron microscopy. After SMAT, nanocrystallites and microtwins were found in the top surface layer. These microstructural features contribute to superior properties of the treated surfaces. Finally, it can be concluded that the mechanical performance of additively manufactured steel under static and fatigue loading can be improved by the SMAT process.

Keywords: additive manufacturing; direct energy deposition; surface treatment; stainless steel; microstructure; low-cycle fatigue

check for updates

Citation: Wegener, T.; Wu, T.; Sun, F.; Wang, C.; Lu, J.; Niendorf, T. Influence of Surface Mechanical Attrition Treatment (SMAT) on Microstructure, Tensile and Low-Cycle Fatigue Behavior of Additively Manufactured Stainless Steel 316L. *Metals* **2022**, *12*, 1425. https://doi.org/10.3390/met12091425

Academic Editor: Pavel Krakhmalev

Received: 11 August 2022
Accepted: 22 August 2022
Published: 29 August 2022

Publisher's Note: MDPI stays neutral with regard to jurisdictional claims in published maps and institutional affiliations.

Copyright: © 2022 by the authors. Licensee MDPI, Basel, Switzerland. This article is an open access article distributed under the terms and conditions of the Creative Commons Attribution (CC BY) license (https://creativecommons.org/licenses/by/4.0/).

1. Introduction

Additive manufacturing (AM), also referred to as 3D printing, is a novel manufacturing process that is capable of fabricating near-net-shape parts with complex geometries in a layer-by-layer manner, directly from the 3D model data, without any molds or tools [1–3]. In a laser-based AM metal process, e.g., laser-based powder bed fusion (PBF-LB) and direct energy deposition (DED), a rasterized laser beam melts the metal powder in a pattern that progressively fills the volume of the designed CAD model and eventually fabricates the metallic part. Selective laser melting (SLM), as one common PBF-LB technique, utilizes the laser to layer-by-layer melt the deposited power bed on the initial substrate plate [4].

DED, also referred to as laser metal deposition (LMD) and laser engineered net shaping (LENS), has been applied for various applications in medical, aerospace, automotive, oil, gas and space industries [5–7]. The DED process can be characterized by the adopted laser

powder, laser type, powder delivery method and feedback control. In the DED process, parts and components are fabricated by focusing a laser beam with high volume energy on the deposition substrate, where the metallic powders are simultaneously delivered and injected by inert gas [6]. The laser and inert gas melt the surface of the previously deposited layer and deliver powder, respectively, to create metallurgical bonding layer by layer in the Z-direction. DED can be used to customize the repair of pre-existing parts, generate components with geometries beyond the capabilities of conventional manufacturing techniques and reduce material wastage significantly by directly depositing the materials with fine precision [8,9]. Furthermore, functionally graded material can be fabricated by adjusting the multi-channel powder feeder or combining powder and wire deposition [10].

The austenitic stainless steel 316L (SS 316L), also known as 1.4404 or X2CrNiMo17-12-2, is used in a wide variety of applications, ranging from nuclear to chemical, petrochemical, marine and offshore oil-related fields, due to its outstanding toughness, ductility and resistance to corrosion [7]. In recent years, there has been an apparently increasing interest in the fabrication of SS 316L by using DED due to its intrinsic advantages mentioned above. Moreover, decreasing prices for metal powder allows DED to substitute other fabrication processes, such as diffusion bonding [11]. A large number of studies have been published investigating the influences of several factors, including process parameters (laser type, laser power, scanning strategy, time interval, preheating temperature), building direction, thickness of the components and powder recycling. Furthermore, surface roughness, residual stress, microstructure and mechanical performance of the additively manufactured SS 316L specimen under quasi-static and cyclic loadings were in focus of those studies [5,7,12–17].

The microstructures of metallic materials determine their macroscopic mechanical properties. The DED process is characterized by a fast heating and cooling rate, which results in a high solidification rate. Thus, often highly directional columnar structures are established, these being characterized by internal substructures, i.e., microstructure refinement [18]. A solidification map showing the effects of temperature gradient and growth rate on the morphology and size of the resulting microstructure can be found in [19,20]. Regarding the whole volume of a deposited component, as a consequence of the complex heat transfer during the DED process, it was reported that the columnar structures are strongly affected by the maximum thermal gradient, where in the last deposited layers, microstructures can be slightly different from the remaining bulk [14].

It is widely agreed that SS 316L fabricated by AM processes is characterized by excellent mechanical properties under monotonic loading, i.e., good ductility and a high yield strength (YS), which is significantly higher compared to specimens that are fabricated by conventional manufacturing techniques, such as hot forging and casting [5,21]. It is believed that the high YS is partly because of the high dislocation density in the AM processed steel. The factors that contribute to the final mechanical properties are the reduced grain and dendrite sizes, the presence of residual δ ferrite and the already mentioned presence of a dense dislocation network (eventually forming substructures of submicron size). These factors can also be used to rationalize the relatively low ductility values sometimes reported for deposited parts. The strengthening effect of the refined microstructure can be correlated with the well-known Hall–Petch equation that associates the material grain size (taking into account the substructures, i.e., dislocation cells) and the yield stress. Detailed comparisons of the microstructure and the mechanical performance among additively manufactured specimens, including DED and SLM, and the ones fabricated by traditional manufacturing methods, such as forging and casting, can be found in [14,17,18].

After manufacturing, additively manufactured metallic components are commonly subjected to post-process heat treatments in order to allow for the elimination of residual stresses and the homogenization of the microstructure. It was found that after heat treatment, the YS and ultimate strength of DED SS 316L were reduced due to the decrease in the ferrite content and the decrease in dislocation density [21,22]. Shot peening has been applied for improving the surface hardness, introducing compressive surface residual stresses

and refining grain size close to the surface, such that the fatigue response of additively manufactured SS 316L specimens could be improved [23].

Surface mechanical attrition treatment (SMAT) is an emerging post-treatment technology among various peening processes, such as ultrasonic peening, laser shot peening and grit blasting, which is capable of inducing a nanostructured layer on the surface of a metallic component and is commonly used in order to improve the fatigue resistance [24–26]. SMAT has been recognized as a technique for upgrading the microstructures and properties of materials by generating a gradient-structured layer on the material surface without tampering with the local chemical compositions and near-surface compressive residual stresses.

In the past few years, numerous studies experimentally revealed that SMAT has a very positive effect on the fatigue behavior of different materials such as steel [27], titanium [28] and magnesium [29] alloys. The AM groups have drawn attention to this surface treatment technique and also applied it to additively manufactured components. Yan et al. [30] have applied SMAT for the modification of the surface layer of Ti6Al4V fabricated by PBF-LB to improve the fatigue performance. It was found that the specimen after SMAT exhibited significantly higher fatigue strength as compared to the non-treated counterparts in both low- and high-cycle fatigue regimes. Sun et al. [31] applied SMAT to PBF-LB-processed stainless steel specimens. The authors showed that the process-induced surface roughness was reduced by up to 96%, such that a surface finish similar to that produced by surface grinding could be achieved. In [32], SMAT was performed on SS 316L parts produced by PBF-LB. It was found that the SMAT treatment can reduce the surface roughness by a factor of 10 and increase the microhardness in the layer beneath the treated surface by up to 45%. The authors further showed that SMAT could also transform the initial near-surface tensile residual stresses present in AM parts into compressive ones and eventually enhance the mechanical properties of the PBF-LB-processed parts [32]. Such studies already demonstrated the potential of SMAT as a post-treatment to improve surface quality and increase the strength while retaining good ductility of PBF-LB manufactured parts.

As the introduction clearly outlines, DED has become an attractive AM technique in numerous fields. However, since many components manufactured by DED are used under very complex loading regimes, often including cyclic loads, the performance under fatigue loading needs to be studied. In this context, mechanical surface treatment processes are often used to improve the fatigue properties of metallic materials. In order to close prevalent research gaps, the present study focused on a unique combination of DED and SMAT. Promising results with respect to the behavior under cyclic loading were expected. To substantiate this expectation, SS 316L components were manufactured using DED. After fabrication, miniature specimens being cut from the components by electro discharge machining (EDM) were surface treated by SMAT. The mechanical performances of as-built and SMAT processed specimens were characterized by monotonic tensile and strain-controlled low-cycle fatigue (LCF) tests. A comparison of the resulting cyclic stress amplitude, half-life hysteresis loops and cyclic hardening/softening was performed for the untreated and SMAT processed specimens. Surface hardness was measured and microstructural features were characterized using electron backscatter diffraction (EBSD) and transmission electron microscopy (TEM) analysis, respectively. The effect of SMAT on microstructural features and the mechanical performance of the DED 316L specimens under static and cyclic loading was comprehensively studied. The macroscopic properties were rationalized in detail based on the microstructure information.

2. Material and Characterization Methods

2.1. Specimen Manufacturing

The SS 316L parts were fabricated using the DED technology at the Dalian University of Technology, China. The system consisted of a Kuka six-axes robot (ZH 30/60III, KUKA, Augsburg, Germany), a Laser Line diode laser generator (LMD 4000-100, Laserline GmbH, Mülheim-Kärlich, Germany) with 4000 W maximum power, a Precitec laser cladding head (YC52, Precitec KG, Gaggenau, Germany) with four coaxial nozzles and a Raychem

metal powder feeder (RC-PGF-D, Raychem RPG Pvt Ltd., Mumbai, India). The powder of SS 316L with a size range of 45-150 µm and a spherical shape, produced by Höganäs (Höganäs, Sweden), was laser deposited on a SS 316L substrate with the dimensions of 130 mm × 40 mm × 15 mm. The nominal chemical composition (in wt.%) of the powder used is given in Table 1. Ar with 99.99% purity was used as a carrier and shielding gas in all processes at flow rates of 400 and 600 L/h. The process parameters adopted are given as follows: laser peak power of 1000 W, scanning speed of 6 mm/s, powder feed rate of 6 mm/s, T-pulse of 25 ms and z-increment of 0.2 mm between two layers for all deposited parts. The dimensions of the components were 60 mm × 10 mm × 40 mm. A bi-directional scanning strategy without rotation between consecutive layers was used. For microstructural and mechanical characterization and SMAT surface treatment, flat dog-bone shaped specimens with nominal gauge section dimensions of 8 mm × 3 mm × 2.0 mm were cut from the initial DED parts by electro-discharge machining (EDM). Further information on the dimensions of the specimen and the actual scanning strategy can be found in Figure 1.

Table 1. Chemical composition of the SS 316L powder used in the present work (wt.%).

Fe	Ni	Cr	Mn	Mo	Nb	Ti	Al	Cu	C	Si
Bal.	12.5	17.1	1.6	2.5	–	–	–	–	0.02	0.7

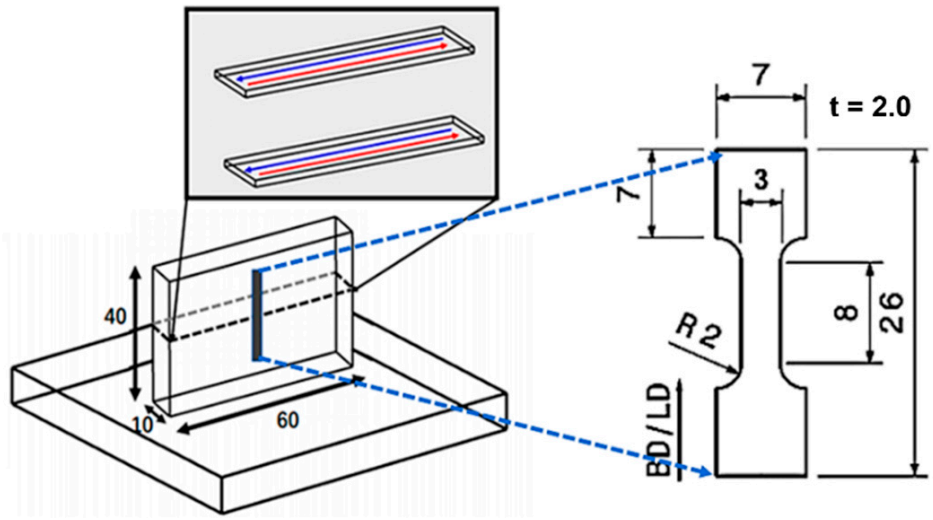


Figure 1. Schematic giving detailed information on the building direction and scanning strategy in the DED process and the dimensions of the specimens (dimensions in mm) cut for SMAT processing.

2.2. SMAT

Upon EDM, some of the DED manufactured SS 316L specimens were subjected to SMAT. No grinding or polishing was conducted between these process steps. The surface treatment was applied to two surfaces of the dog-bone shaped specimens cut from the initial DED cuboids (cf. Figure 1). Figure 2 shows a schematic diagram of the SMAT system. As can be deduced from the schematic, the major part of the specimen's surface, except for 1 mm of the clamping section on each side, was processed by SMAT. In the SMAT process, a chamber was attached to the vibrator, and spherical balls (304 stainless steel + ZrO2) with a diameter of 3 mm were placed inside the sealed chamber. During the SMAT process, the specimen secured to the top of the chamber was impacted by the spherical balls driven by the vibrations of the chamber attached to the vibrator. The same procedure was separately performed on the two large surfaces of each specimen. During SMAT processing of one side of the surface, the opposite side was completely fixed (cf. Figure 2). Due to the size of the spherical balls used, partial SMAT co-processing of the side surfaces of the specimen can be excluded. The vibration frequency and amplitude were electromagnetically controlled

by a signal generator and an amplifier. The repeated impacts of spherical balls at a high speed and a high frequency can cause indentation and plastic deformation on the treated surface of a specimen. In the present work, the AM processed specimens were treated for 1 h at a vibration frequency of 20 Hz. After SMAT processing, no further grinding or polishing was conducted prior to mechanical testing. This also held true for the as-built counterpart condition.

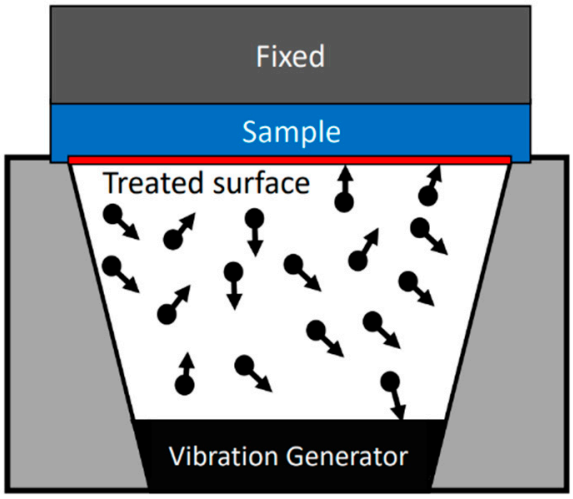


Figure 2. Schematic highlighting the most important features of the SMAT system.

2.3. Mechanical and Microstructure Characterization

Surface roughness measurements were conducted using a Mitutoyo SJ-210 (Mitutoyo, Kawasaki, Japan). Five readings within a specimen length of 0.8 mm were recorded on the large surfaces of the specimen directly in the gauge length. The roughness values R_a reported represent average values calculated from all readings. Characterization of mechanical properties comprised hardness investigations as well as tensile and fatigue tests. Vickers hardness testing was carried out using a Struers DuraScan-70 system (Struers, Copenhagen, Denmark) employing a load of 4.9 N. A screw-driven MTS criterion load frame with a maximum load capacity of 20 kN was used to perform uniaxial tensile tests under displacement control with a constant crosshead speed of 2 mm/min. Strain measurement was conducted using an MTS miniature extensometer with a gauge length of 5 mm directly attached to the surface of the specimen. The same extensometer was used for strain control during the LCF tests, performed in fully reversed push–pull loading ($R_\varepsilon = -1$). A constant strain rate of 6×10^{-3} s^{-1} and total strain amplitudes of $\Delta\varepsilon_t/2 = \pm 0.2\%$, $\Delta\varepsilon_t/2 = \pm 0.35\%$ and $\Delta\varepsilon_t/2 = \pm 0.5\%$ were used. The fatigue investigations were performed on a digitally controlled servo-hydraulic load frame with a maximum force capacity of 16 kN. In total, three tensile tests and two fatigue tests were performed for each condition.

Microstructure analysis of as-built DED specimens—i.e., investigation of grain size and grain morphology—was conducted using a Zeiss ULTRA GEMINI high-resolution SEM (Carl Zeiss AG, Oberkochen, Germany) operating at an acceleration voltage of 20 kV. The SEM was equipped with an electron back-scatter diffraction (EBSD) unit and a back-scattered electron detector. For EBSD measurements, all specimens were mechanical ground down to 5 µm grit size using silicon carbide (SiC) paper, and vibration polished for 16 h using a conventional oxide polishing suspension (OPS) with a grain size of 0.04 µm. The measurements were performed using two different magnifications (100× and 500×) and step sizes (1 and 0.2 µm). The EBSD data analysis was performed with the Bruker Esprit 2.3 software (Bruker, Billerica, MA, USA).

Detailed microstructure analysis of as-built and SMAT processed specimen was additionally conducted by TEM using a JEM 2100PLUS system (JEOL, Freising, Germany) operated at 200 kV. TEM foils were selected from different local regions, i.e., close to the

surface and in the center of the specimen. The TEM foils were prepared by focused ion beam (FIB) using a FEI Helios NanoLab 600i DualBeam SEM/FIB system (FEI, Hillsboro, OR, USA) operated at 30 kV.

3. Results and Discussion

3.1. Microstructural Analysis of As-Built Specimen by SEM

In the DED process, the thermal history during processing plays a crucial role in establishing specific microstructural features, e.g., morphology and grain size. In general, the microstructure is determined by the solid–liquid interface velocity R, the thermal gradient G and the alloy composition. In particular, the solidification morphology parameter (G/R) and the cooling rate level G×R define the solidification mode, and therefore, the microstructure morphology and its inherent dimensions. In general, as-built DED specimens were characterized by an obvious solidification pattern on the macroscopic scale and cellular substructures on the microscopic scale [12]. In conventionally processed but rapidly cooled austenitic stainless steel, depending on its chemical composition, two different microstructural constituents can be found: austenite γ and the so-called ferrite δ [18].

Figure 3a shows a representative EBSD inverse pole figure (IPF) map. The measurement depicted was performed in the clamping section of a SS 316L specimen (cf. Figure 1). The grain orientations of the EBSD micrograph are plotted with respect to the build direction (BD). The microstructure exhibits large columnar grains with a length of up to 300 µm and width of about 100 µm, respectively. No obvious melt pool boundaries are noticeable. DED can be considered as a directional solidification process characterized by a high temperature gradient and rapid cooling rate. Thus, the grains are mainly orientated in the building direction; however, they are characterized by a slight shift towards the laser travel direction (LTD). This observation was similarly made in previous investigations on DED SS 316L [33] and can be explained by the local conductive heat transfer, i.e., the direction of heat flux. It can further be seen that the SS 316L specimen in the as-built condition was characterized by slightly increased texture intensity in BD. The IPF map is characterized by a comparatively increased fraction of {101}-oriented grains. In these cases, the grains grow parallel to the thermal gradient and direction of heat flux, with a growth rate, which is strictly related to the scan speed used during the building process. The slightly increased texture intensity is additionally highlighted by the IPF displayed in Figure 3e, extracted from the EBSD data of the micrograph shown in Figure 3a. A similar texture evolution was also reported by Andreau et al. [34] for PBF-LB-processed 316L parts. Most importantly, it has to be noted that the process parameters, including laser powder, scan speed, and scanning strategy, significantly influence the size and shape of the melt pool, which in turn affects the resulting texture and grain morphology [3]. However, further in-depth texture investigations, including X-ray diffraction analysis, across the entire part built, have to be conducted in order to analyze the texture's evolution in more detail. In literature, solidification maps have been successfully used for assessing the effects of temperature gradient and growth rate on the morphologies and sizes of microstructural features [19,20]. Figure 3b shows a magnified view of the marked white dashed rectangle in the IPF map in Figure 3a. From the variations in the color within the grains, the presence of subgrains and lattice distortions can be deduced. This is in line with the observations made by Belsvik et al. [33] with respect to the microstructure evolution in DED-processed SS 316L-Si. In addition, some non-indexed areas can be noticed in the magnified IPF map in Figure 3b. From the corresponding image quality map in Figure 3c, these areas can be identified as distinct boundaries inside the grains. Figure 3d shows a phase map of a magnified area of the image quality map in Figure 3c. From this map, the boundaries can be identified as phase-boundaries. In the study of Belsvik et al. [33], a volume fraction of about 2.5% δ-ferrite on the interdendritic and subgrain boundaries was determined by EBSD analysis. In another study [35] investigating the stress corrosion cracking susceptibility of 304L substrate and 308L weld metal exposed to a salt spray, the authors showed that in a

conventional fusion weld δ-ferrite can be formed intra- and inter-granularly. The presence of δ-ferrite in DED-processed SS 316L was additionally reported by Saboori et al. [14] based on X-ray diffraction data. From the phase map shown, minor amounts of ferrite can be observed. Generally, the presence and amount of δ-ferrite formed in SS 316L were discussed by Bedmar et al. [18]. In their study reporting on a comparison of different AM methods for 316L stainless steel, a Schaeffler diagram was used to predict the phases based on the chromium and nickel equivalent when the cooling was not in full equilibrium, as is the case in AM and conventional welding. For SS 316L, austenite with a fraction of 5–10% of δ-ferrite was predicted. According to the findings of the EBSD measurement shown in Figure 3d, a volume fraction of about 2% was observed for the DED SS 316L condition of the present study. This in line with the results from Belsvik et at. [33] reporting on a volume fraction of about 2.5% δ-ferrite determined by EBSD. According to [33], differences compared to the theoretical value may be related to poor statistics of the quantitative analysis. As stated in [18], in welding, the presence of a 5–10% δ-ferrite phase improves the behavior of austenitic steels. Moreover, values above 10% lead to reductions in ductility, toughness and corrosion resistance whereas values below 5% can cause solidification cracking. As a result, the presence of 2% δ-ferrite could degrade the properties of the DED SS 316L specimens. However, traces of solidification cracking were not found in the present work.

3.2. Microstructural Features on the Nano-Scale

Figure 4 shows the microstructural evolution within specific regions close to the top surface layer for a specimen which was subject to SMAT processing. Figure 4a shows a gradient structure (in terms of the grain size) in the probed region close to the top surface (marked as layer 1 in the schematic depicted in Figure 6). Figure 4b shows the specific microstructure of the area marked by a red rectangle in Figure 4a, whereas Figure 4c shows the corresponding SAED pattern revealing the presence of a polycrystalline structure (single spots are labelled for clarity). It can be clearly seen that nanograins formed in the region close to the top surface layer (≈0.025–0.05 mm), consistently with the TEM bright field image in Figure 4b. This observation is in line with the literature reporting on SMAT processed SS 316L. According to Tao et al. [36], strain-induced grain refinement and martensite transformation can take place in the top surface layer during SMAT. The grain sizes of the nanocrytallites formed were reported to be in the range of 8 to 60 nm with a mean value of about 30 nm, which correspond well with the results shown in Figure 4b. The authors further reported that the grain refinement in SS 316L after SMAT processing can be attributed to the formation of planar dislocation arrays and mechanical twins; a grain subdivision by mechanical twins and martensite transformation; or the formation of nanocrystallites [36]. Generally, as a result of mechanical surface treatment processes, the elastic-plastic deformation leads to severe local shearing of the surface layer, including activation of dynamic recrystallisation, and thus to grain refinement down to the nanometer range [37,38]. With increasing distance from the specimen surface (≈ 0.1–0.15 mm), e.g., within layer 2 in the schematic in Figure 6, differences in the microstructure became obvious by TEM nano-scale analysis. Figure 4d,e shows bright-field and dark-field TEM images of a nanotwinned microstructure, respectively. Figure 4f shows the corresponding selected area electron diffraction (SAED) pattern, clearly revealing the presence of deformation-induced twins. The austenite matrix and the nano-scaled deformation twins are indexed in the diffraction pattern. In accordance with these observations, Tao et al. [36] reported that at a distance from the treated surface of 30–40 μm, lamellar structures with a width of approximately less than 100 nm were formed, which can be attributed to the evolution of nano-sized mechanical twins. Twinning in SS 316L as a result of surface treatment processes was also shown for other processes. Agrawal et al. [39] reported multiple twin systems resulting in the formation of a dense crisscrossed twin structure by using the novel vaporizing foil actuator (VFA) technique. Wang et al. [40] studied the microstructural evolution and the mechanical behavior of 316L parts after surface treatments by ultrasonic impact peening (UIP) and laser shock peening (LSP). The authors reported that mechan-

ical twinning was almost completely absent in the specimen processed by UIP, whereas twinning was frequently observed in specimens treated by LSP. It was concluded that the magnitude of peak pressure determined the transition from a dislocation-dominated mechanism (≈680 MPa for UIP) to a twinning-dominated mechanism (≈2200 MPa for LSP). Thus, it can be assumed that the peak pressure induced by the SMAT treatment in the current study was high enough to induce twinning in the surface treated region.

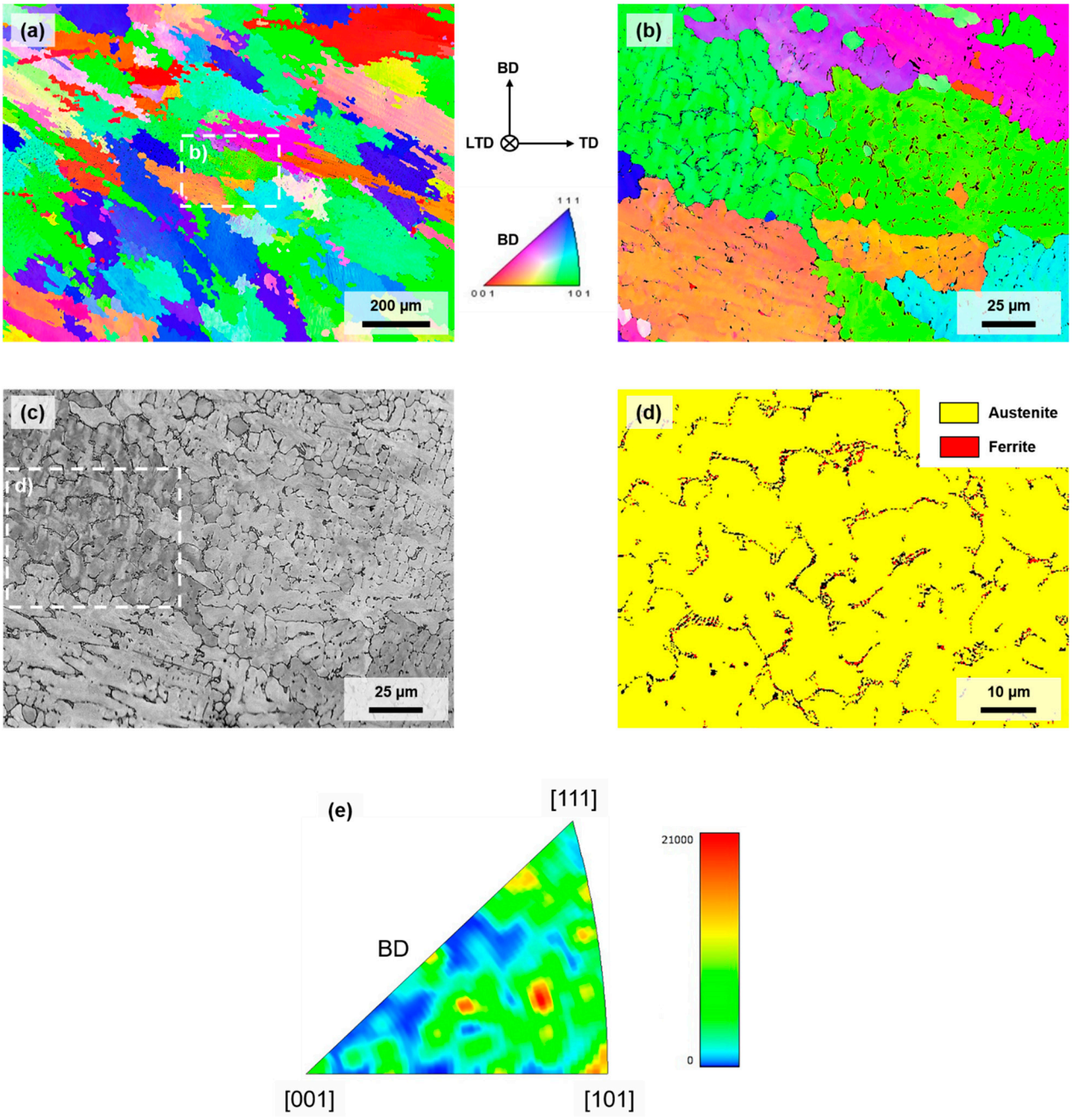


Figure 3. (**a**) EBSD inverse pole figure (IPF) map of an as-built DED SS 316L specimen. (**b**) A magnified view of the marked white dashed rectangle in (**a**). (**c**) Image quality map highlighting the grain structures in addition to the IPF map in (**b**). (**d**) EBSD phase map of the marked white dashed rectangle in (**c**). The grain orientations in (**a**,**b**) are plotted with respect to the build direction (BD). (**e**) Inverse pole figure calculated from EBSD data of the micrograph shown in (**a**) revealing the micro-texture of the DED SS 316L. Data are plotted with respect to the BD.

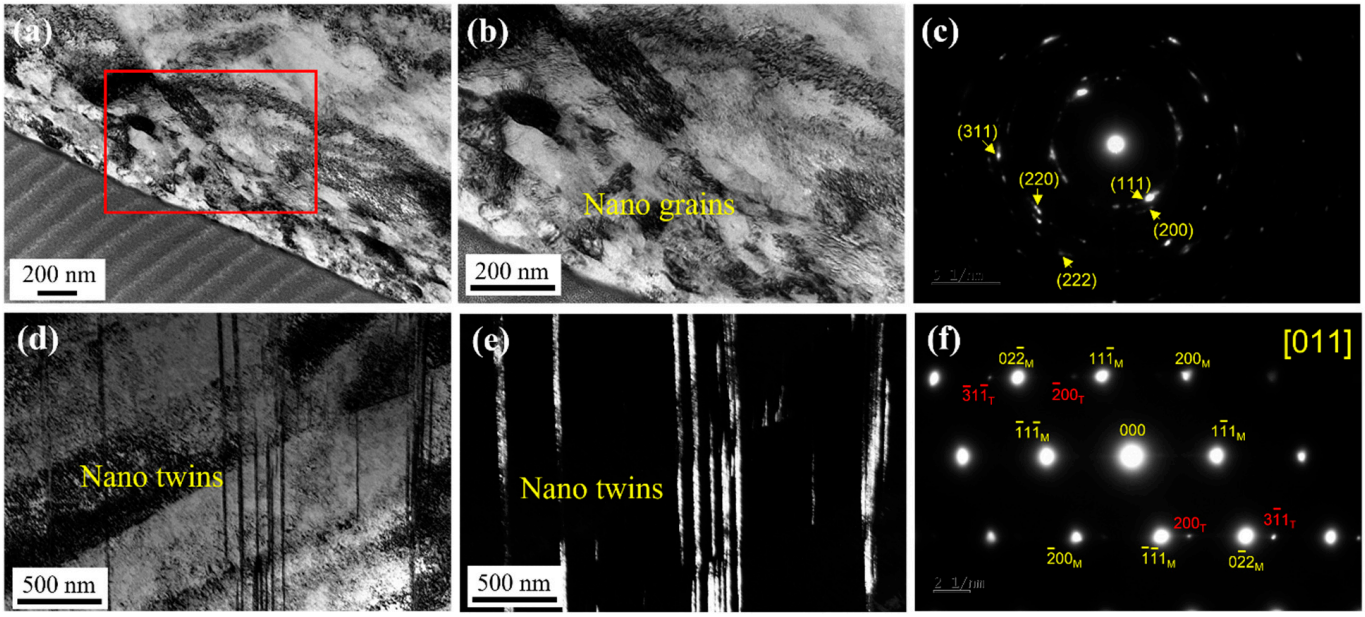


Figure 4. TEM micrographs of regions adjacent to the top surface layer of the SMAT processed condition of the SS 316L specimen and magnified view of a selected locations: (**a**) bright-field image of a nano-grained layer; (**b**) higher magnification micrograph of nanograins in the region marked by the red rectangle in (**a**); (**c**) SAED of nanograins; (**d**) bright-field image showing nanotwins and slip bands, (**e**) dark-field image highlighting the nanotwins; (**f**) SAED of the nanotwins.

In addition to the formation of nanocrystallites and deformation-induced twins, deformation-induced martensite was found in the surface treated layer in some studies reporting on mechanically surface-treated SS 316L. Jayalakshmi et al. [41] reported on a gradient nanostructured layer after severe shot peening. The initial hot-rolled austenitic microstructure, being characterized by grain sizes in the range of 40–80 µm, was refined to a dislocation cell-type structure with deformation-induced martensitic structures having cell sizes in the range of 100–140 nm. The authors showed that the martensite, assessed by TEM investigations, was nucleated at multiple locations in the austenite matrix. However, with the measurement methods used in the present study, no martensitic transformation could be observed. The diffraction spots of the SAED pattern shown in Figure 4f, associated with Figure 4d,e, clearly correspond to the austenite phase, additionally revealing twin reflections. The lath-like microstructure appearance in Figure 4d might thus be attributed to the formation of shear bands. In a study reporting on the microstructural evolution of SS 316L subjected to SMAT treatment, Bahl et al. [42] showed that microbands and shear bands were formed as a result of SMAT processing. The authors further concluded that deformation twinning and dynamic recrystallization within the shear bands are responsible for nanocrystallization.

With a further increase in the specimen depth analyzed, i.e., at a larger distance to the treated surface, Figure 5a,b shows TEM bright-field images of the local microstructure (in a distance from the surface of approximately 1.0–1.2 mm corresponding to layer 3 in Figure 6). From both micrographs, it can be deduced that within the investigated region, dislocation cell walls (marked by the yellow arrows) were formed during the SMAT processing. As will be pointed out by the results of hardness investigations in Section 3.3 (cf. Figure 7), the area under investigation in Figure 5 corresponded to the non-affected as-built DED microstructure. This specific microstructure was in good agreement with data available in literature. In their study investigating the origin of dislocation structures in an additively manufactured austenitic SS 316L, Bertsch et al. [43] reported that the highest dislocation densities were found in DED 3D and PBF-LB parts, manifested in the formation of dislocation cells approximately 300–450 nm in diameter. The authors further showed that dislocation structures in AM originated as a consequence of thermal distortions during

processing, which were primarily dictated by constraints surrounding the melt pool and thermal cycling, respectively.

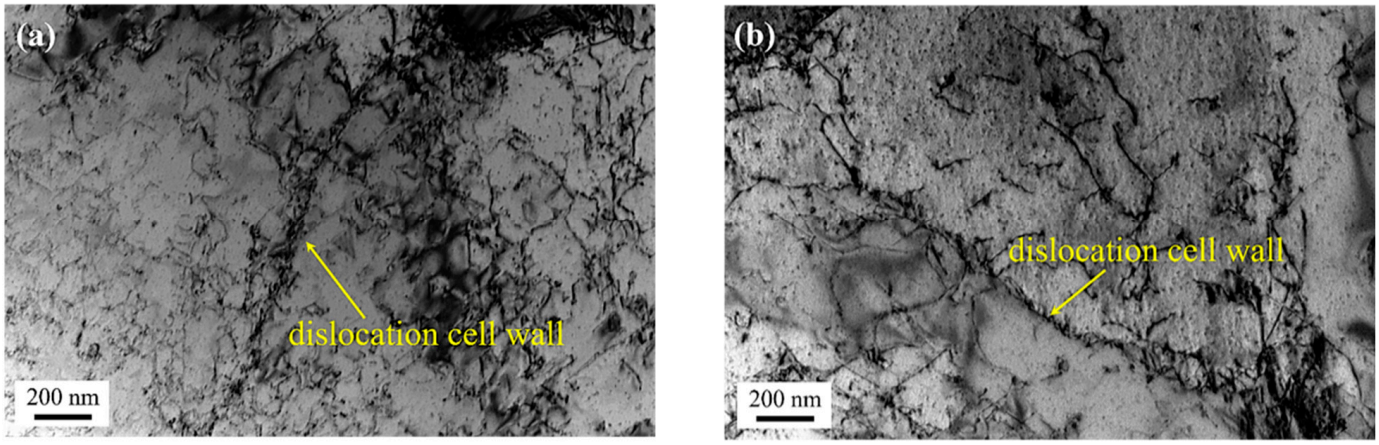


Figure 5. (**a**,**b**) Representative bright-field TEM micrographs of the center part of a SMAT processed SS 316L specimen.

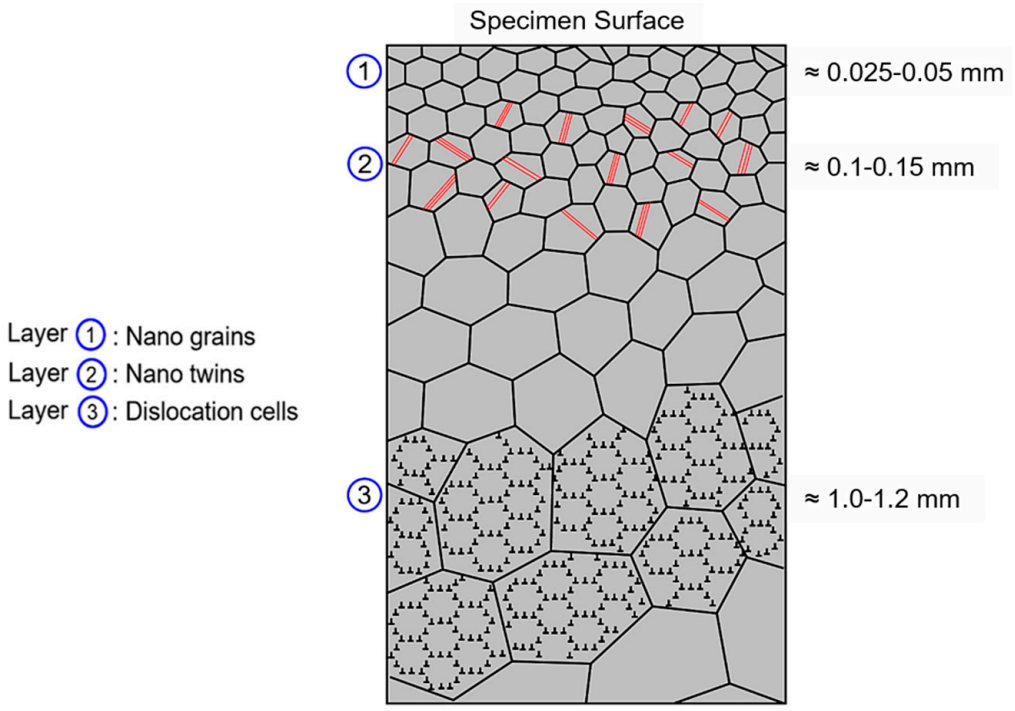


Figure 6. Schematic of the cross-sectional microstructure of the SMAT processed SS 316L specimen consisting of a nanograin layer adjacent to the top surface, a nanotwin layer below the nanograin layer and a layer characterized by dislocation cells in the central region.

The results obtained by TEM nano-scale analysis are summarized in the schematic of the cross-sectional microstructure of a SMAT processed SS 316L specimen displayed in Figure 6. As is obvious, the specimen was characterized by various types of microstructures after surface treatment, being explicitly characterized by the gradually increasing grain size with an increasing distance to the surface. In the immediate vicinity of the surface, i.e., a depth of ≈0.025–0.05 mm, nanocrystallites were found, whereas with increasing distance to the surface (≈0.1–0.15 mm), mechanically induced nanotwins with a mean thickness of approximately 100 nm were observed within the deformed grains. As reported in [34], such a gradient microstructure including randomly-oriented equiaxed nanocrystallites in the top surface layer and mechanical nano-sized twins below this layer were also found for Inconel

600 specimens following SMAT surface treatment. In the central region (≈1.0–1.2 mm), i.e., in the non-surface treated bulk material, the microstructure was characterized by high density of dislocation cells formed within the coarse grains directly stemming from the DED process.

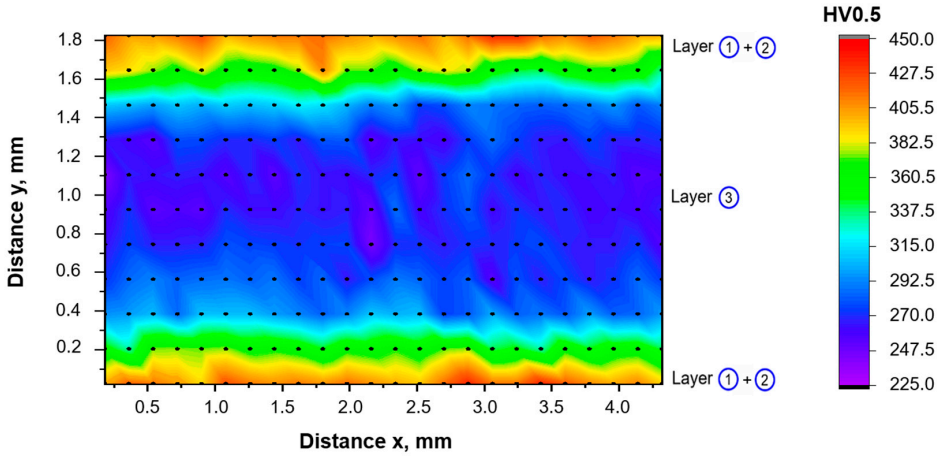


Figure 7. Hardness map showing the hardness distribution in the cross-section of a SMAT processed SS 316L specimen. Each black dot represents the position of a single measurement. The different microstructural layers characterized by TEM measurements (cf. Figure 6) are also marked.

3.3. Roughness, Hardness and Mechanical Response under Tensile Loading

Depending on the initial surface appearance before the SMAT treatment, the roughness profile can either be improved or deteriorated [32,44]. In order to analyze the effect of SMAT, surface roughness measurements were carried out on the large surfaces of specimens from both conditions considered. While the as-built condition after EDM was characterized by an average roughness R_a of 3.84 µm, smoothing of the surface can be observed after the SMAT treatment, revealing an average roughness value of 1.40 µm. This is in line with the investigations of Portella et al. [32] reporting that the surface roughness of as-built SLM parts was considerably reduced by a SMAT post-treatment.

In order to analyze the effective depth of a specimen being influenced by the SMAT surface treatment, Vickers hardness measurements were carried out on a cross-section of a specimen cut from the clamping area. In total, 264 individual measurements were carried out. The results obtained are illustrated in the hardness map in Figure 7. The position of each measurement point is represented by a black dot. Additionally, 10 measurements were carried out in the clamping section of a non-surface treated specimen in order to determine the mean value of the hardness after the DED process. As a result of these measurements (results not shown in Figure 7), the medium hardness of a specimen without SMAT was found to be approximately 237.7 HV0.5, whereas the maximum and minimum values were determined to be 227 and 247 HV0.5, respectively. A similar hardness can also be derived for the central area of the cross-section of a SMAT processed specimen from the hardness map in Figure 7. In contrast, an increase in hardness can be seen for the near-surface layer of each SMAT processed surface. In fact, in the direct vicinity of the treated surface the hardness was increased by a factor of about two, reaching maximum values of up to 450 HV0.5. Taking the results of the nano-scaled microstructural investigations into account, the increased hardness in direct vicinity of the surface can be attributed to the formation of the nanocrystallites, and thus to the intense level of grain refinement in this area. This observation can be explained based on the well-known Hall–Petch relation, according to which the increase in hardness or strength is inversely proportional to the square-root of the mean grain diameter [45]. Although an increase in grain sizes was observed with a concomitant increase in the distance to the surface, this area was still characterized by a higher mean hardness of approximately 375 HV0.5 as compared to the central region. This observation can be attributed to the formation of the mechanically

induced nano-sized twins in this area. The formation of these twins by the SMAT treatment led to the so-called dynamic Hall–Petch effect, i.e., an increasing density of interfaces within the grains eventually, promoting the increase in hardness [46,47]. The hardness map further demonstrates that the SMAT treatment is characterized by an effective depth of approximately 0.5 mm (on both sides of the specimen), as this is the range, the hardness converges to the values obtained for a non-surface treated specimen before. Taking the nominal specimen thickness of 2.0 mm into account, it can be concluded that almost 50% of the cross-sections of the specimens considered in present work were strengthened by the SMAT process.

Figure 8 highlights the behavior under quasi-static tensile loading by depicting representative stress–strain curves of the as-built and SMAT processed SS 316L specimens. The mechanical response of the as-built specimen was characterized by well-defined elastic–plastic behavior, a YS of approximately 300 MPa, an ultimate tensile strength (UTS) of 715 MPa and an elongation at fracture of 19%. With respect to the SMAT processed specimen, the mechanical performance and quasi-static tensile strength were characterized by the following values: YS of 375 MPa, UTS of 800 MPa and elongation at fracture of approximately 6.5%. It can be derived that the value of the YS of the SMAT processed specimen is 25% higher than that of the as-built counterpart. Compared to SS 316L counterparts produced by conventional methods (casting and forging) [48], the as-built DED-processed specimen considered in the present study was characterized by increased YS and UTS values. This fact can be attributed to the unique microstructure of the alloy generated by the AM process. As a consequence of the process's inherent rapid cooling rates, a finer microstructure compared to conventional counterparts with subgrain structures evolves. The formation of δ-ferrite in the DED SS 316L (in the intergranular regions) further strengthens the soft austenitic matrix. Concomitantly, a reduction in the ductility could be observed in comparison with the cast and forged counterparts [48]. In addition, dislocation cells were detected in the non-surface treated microstructure by nano-scale microstructure analysis. The improved mechanical strength of additively manufactured metals has been attributed to the formation of these dislocation cell structures with solute micro-segregation [49,50]. In contrast, the increase in the strength after SMAT processing can be attributed to the volume of material affected by the surface treatment. As evidenced by the hardness map, almost 50% of the cross-section was strengthened by SMAT, explaining the increased strength and more pronounced brittleness. An increase in the strength under monotonic tensile loading and a simultaneous reduction in ductility, have often been reported for other austenitic steels after mechanical surface treatment [46,51].

3.4. Low-Cycle Fatigue Analysis

In this section, the LCF properties of the DED SS 316L are presented and analyzed for the as-built and SMAT processed (applied to the two large surfaces of each specimen) conditions. Figure 9 shows the cyclic deformation responses (CDRs) for the conditions considered, i.e., as-built and SMAT. The LCF tests were conducted at various total strain amplitudes—i.e., Figure 9a, $\Delta\varepsilon_t/2 = \pm 0.2\%$, Figure 9b; $\Delta\varepsilon_t/2 = \pm 0.35\%$; and Figure 9c, $\Delta\varepsilon_t/2 = \pm 0.5\%$. As mentioned in Section 2, two tests were conducted for each condition in order to analyze the reproducibility and scatter behavior of the LCF response. As, with respect to resulting stress amplitudes and number of cycles to failure, no pronounced scatter was detected, only one curve for each condition and loading condition is shown for the sake of clarity. In order to avoid buckling of the miniature specimen, the load was increased stepwise during the first cycles. As a result, the prescribed strain amplitude was reached after approximately 10–50 cycles, depending on the actual strain amplitude. Thus, these initial cycles were not taken into account for evaluation. From the CDRs depicted, it can be deduced that, irrespective of the condition, a higher imposed strain amplitude resulted in higher cyclic stress amplitudes and decreased fatigue life. Furthermore, for a given total strain amplitude, the resulting cyclic stress amplitudes of the SMAT processed specimens were slightly increased compared to those of their untreated counterparts. The

hardening/softening behavior, which is characterized by an increase or decrease in the corresponding stress response throughout the fatigue tests, can also be derived from the graphs shown in Figure 9. The CDRs of both conditions are characterized by similar courses for all total strain amplitudes considered. After reaching the prescribed strain amplitude, a slight initial saturation stage is followed by cyclic softening being more pronounced at higher total strain amplitudes and for the SMAT processed specimens in direct comparison to their as-built counterparts. The cyclic softening behavior presumably results from the rearrangement of dislocations and a decrease in the overall dislocation density, as similarly shown in previous studies [52–54]. As revealed by the TEM measurements, fast-cooling and the repeated cyclic heating during the DED processing promoted the formation of dislocation cell walls (cf. Figure 5) in the as-built microstructure. Obviously, the more pronounced softening during cyclic loading, as deduced from the CDRs of the SMAT condition, caused an even higher (local) dislocation density after surface treatment (cf. layer structure shown in Figure 6). Regarding number of cycles to failure for the two conditions considered, a change in the properties can be deduced from the CDRs depicted in Figure 8. While fatigue life at the lowest total strain amplitude of $\Delta\varepsilon_t/2 = \pm 0.2\%$, i.e., about 110,000 cycles for the SMAT condition, is more than 25% higher than for the as-built counterpart (≈80,000 cycles), this trend changes with increasing strain amplitude. For the medium total strain amplitude, i.e., $\Delta\varepsilon_t/2 = \pm 0.35\%$, the as-built condition is already characterized by an increased number of cycles to failure of approximately 40%, whereas for the highest total strain amplitude of $\Delta\varepsilon_t/2 = \pm 0.6\%$, the fatigue life is, with ≈3.400 cycles, more than two times higher than that of the SMAT counterpart (≈1.400 cycles). These observations can be explained based on the characteristics of the surface treated conditions. In line with several other surface treatment processes, such as shot peening and deep rolling, SMAT is well known for establishing nanocrystalline near-surface layers characterized by high compressive residual stresses and increased hardness due to work hardening. Depending on the initial surface appearance before SMAT treatment, the roughness profile can either be improved or deteriorated. In addition, deformation-induced twinning or phase transformation can be triggered as a result of the high plastic deformation [32,44,55]. According to [56], the cyclic deformation responses of surface-strengthened specimens are characterized by lower plastic strain amplitudes over the number of cycles due to the residual stresses present and the effective strengthening of the near-surface layer. In order to achieve a permanent improvement in the general performance imposed by these characteristics, the stability of the near-surface layer properties is of decisive importance. However, stability can be detrimentally influenced by thermal and mechanical (quasi-static and/or cyclic) stresses and strains [57]. Figure 10 depicts half-life hysteresis loops for both conditions and all total strain amplitudes considered. The area of a hysteresis loop represents the energy dissipation per cycle and is directly related to the plastic strain amplitude, i.e., half of the maximum width of the hysteresis curve. An increased energy dissipation per cycle can be linked to a more intense dislocation activity, eventually promoting premature failure [53,58]. As can be deduced from Figure 10a for the lowest total strain amplitude of $\Delta\varepsilon_t/2 = \pm 0.2\%$, the SMAT condition's outcomes are characterized by a narrower half-life hysteresis loop, i.e., a lower plastic strain amplitude due to characteristics of the near-surface layer, as described above, resulting in a higher number of cycles to failure as compared to the as-built counterpart. As the hysteresis loop of the SMAT samples is almost fully closed, revealing only a very low contribution of plastic strain, relatively high stability of the near-surface layer properties could be expected. After increasing the total strain amplitude, the appearance of the half-life hysteresis loops changes. For the medium total strain amplitude, the differences in the plastic strain amplitudes of both conditions start to decrease, revealing only a slightly wider opened hysteresis for the as-built condition, but the hysteresis loops become almost equal for the highest total strain amplitude of $\Delta\varepsilon_t/2 = \pm 0.5\%$ (cf. Figure 10b,c). As a common feature of both total strain amplitudes, all half-life hysteresis loops are characterized by a pronounced contribution of plastic strain irrespective of the condition considered. From these results it can be concluded that with increasing total

strain amplitude, and thus increasing plastic deformation, the near-surface layer properties become instable and lose their effect. In general, at high plastic strain ranges, i.e., in the LCF regime, materials of higher ductility have a higher crack-initiation resistance, and thus, superior fatigue life. On the contrary, at low plastic strain ranges, i.e., in the high-cycle fatigue (HCF) regime, materials of higher tensile strength are characterized by higher crack-initiation and growth resistance. In conclusion, the fatigue resistance in different regimes comprises a tradeoff among strength and ductility in dependence of the plastic strain evolution [59]. Thus, the improved fatigue life of the as-built DED SS 316L condition at medium and high total strain amplitudes, deduced from the CDRs in Figure 9, can be rationalized by higher ductility compared to the SMAT counterparts (cf. Figure 8) in combination with the degrading near-surface layer properties of the surface treated SMAT condition. In contrast, the stability of the properties induced by SMAT and the generally improved strength lead to improved cyclic properties at low total strain amplitudes. Thus, the results of the present study already indicate that a significant improvement in the cyclic properties in the HCF regime, known to be characterized by crack initiation and failure mainly due to elastic deformation [60,61], can be expected for the SMAT DED SS 316L.

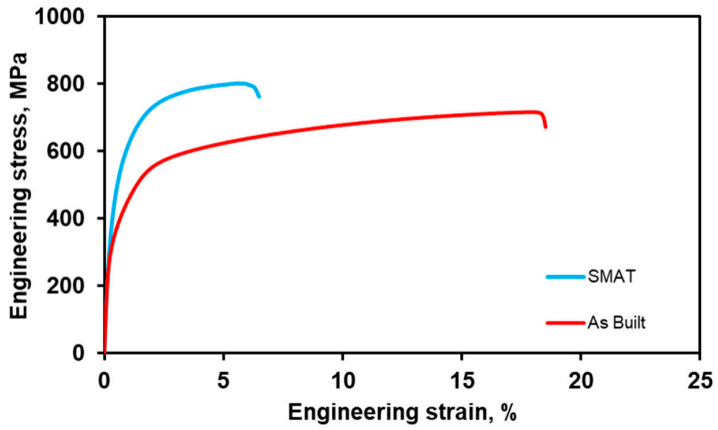


Figure 8. Representative tensile stress–strain curves of as-built and SMAT processed SS 316L specimens.

3.5. Fracture Surface Analysis

After fatigue testing, fracture surface analysis was carried out for all specimens tested. The SEM micrographs obtained for the highest total strain amplitude, i.e., $\Delta\varepsilon_t/2 = \pm 0.5\%$, are shown in Figure 11. As, irrespective of the condition, similar characteristics were revealed for specimens fatigued at all strain levels, the depicted fracture surfaces can be considered as representative. Thus, for sake of brevity, micrographs for only one total strain amplitude are shown. From the fracture surfaces presented, well-known features for fatigue tested specimen can be deduced. Besides areas of fatigue crack initiation (cf. Figure 11b,d) and propagation characterized by submicron fatigue striations, the fracture surfaces of both conditions are characterized by an overload final fracture region with a ductile, dimple-like structure (cf. Figure 11c,f). In line with the number of cycles to failure being increased by more than a factor of two for the as-built condition compared to the SMAT counterpart, an increase in the share of the area characterized by stable fatigue crack propagation can be observed. In addition, the fracture surface of the as-built condition locally seemed to be plastically deformed to a higher extent. This fact can be explained by the higher ductility, as already deduced from the results of the tensile tests (cf. Figure 8). As common feature of both conditions, fatigue crack initiation was always located on the side surface of the specimen, marked by the white arrows in Figure 11a,d. In general, a typical characteristic known from the literature related to mechanical surface treatment processes such as shot peening and deep rolling, is a shift of the crack initiation points away from surface areas towards internal defects. This is a result of the near-surface compressive residual stresses [27,51,62,63]. This has previously been shown in other fatigue studies on SMAT processed materials as well [30,64]. However, as detailed in Section 2.2, SMAT was

only performed on the two large surfaces of each specimen in order to gain initial insights into the impacts of this emerging surface treatment process with respect to microstructural evolution and effective depth. Since fatigue cracks for the SMAT condition in the present work always initiated from the surface of the specimen, even for the lowest total strain amplitude of $\Delta\varepsilon_t/2 = \pm 0.2\%$ (not shown for sake of brevity), it can be assumed that the non-treated side surfaces represented the weakest link under fatigue loading. As a result, the conditions in focus in the current study, i.e., as-built and SMAT processing, result in similar crack initiation behavior. Due to the increased brittleness of the SMAT processed samples (cf. Figure 8), a higher crack growth rate can be assumed, eventually leading to premature failure of the specimen compared to the as-built counterpart, at least at medium and high total stain amplitudes characterized by high plastic strains. The positive influence of SMAT treatment at the low strain amplitude can be rationalized based on a surface-core model (in accordance with the well-known Masing model [65,66]). Due to the significant volume fraction of the deformed surface layers, the composite body of surface and core only suffered decreased plastic strain amplitudes (cf. Figure 10). After exceeding the YS of the unaffected core to a much higher degree in the case of the higher strain amplitudes, the local plastic strain for the surface layer was also increased. From the results presented, it can therefore be concluded that for an effective impact of a SMAT treatment, either rotationally symmetrical components should be used or a flat specimen should be processed on all surfaces. Otherwise, non-treated sides can be considered as weak points under cyclic loading, especially at high plastic strains.

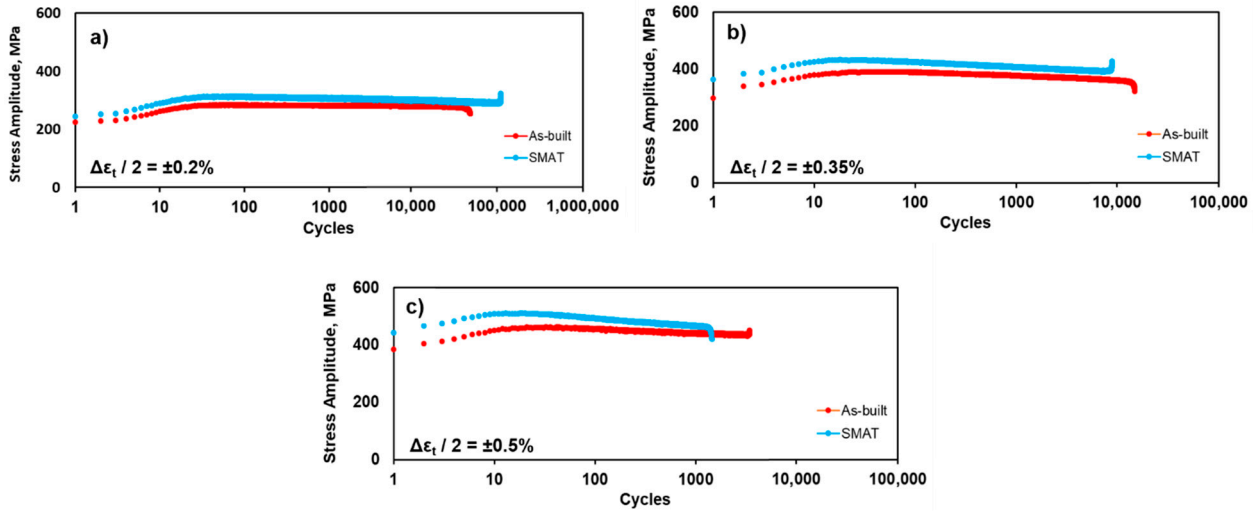


Figure 9. Cyclic stress response at room temperature at total strain amplitudes of (**a**) $\Delta\varepsilon_t/2 = \pm 0.2\%$, (**b**) $\Delta\varepsilon_t/2 = \pm 0.35\%$ and (**c**) $\Delta\varepsilon_t/2 = \pm 0.5\%$ for the DED SS 316L in as-built and SMAT processed condition.

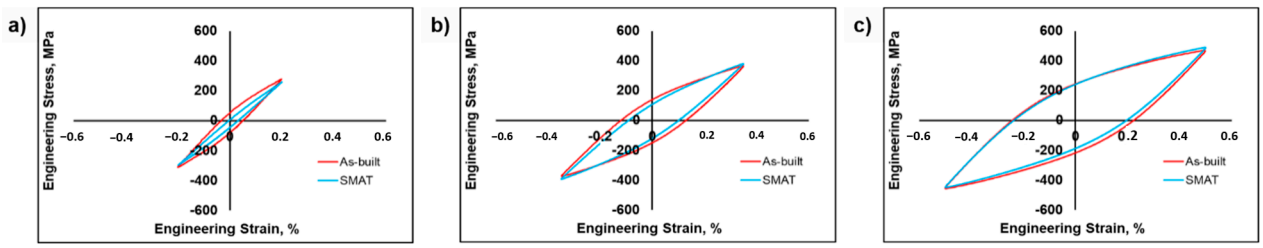


Figure 10. Half-life hysteresis loops for the DED SS 316L in as-built and SMAT processed conditions for total strain amplitudes of (**a**) $\Delta\varepsilon_t/2 = \pm 0.2\%$, (**b**) $\Delta\varepsilon_t/2 = \pm 0.35\%$ and (**c**) $\Delta\varepsilon_t/2 = \pm 0.5\%$.

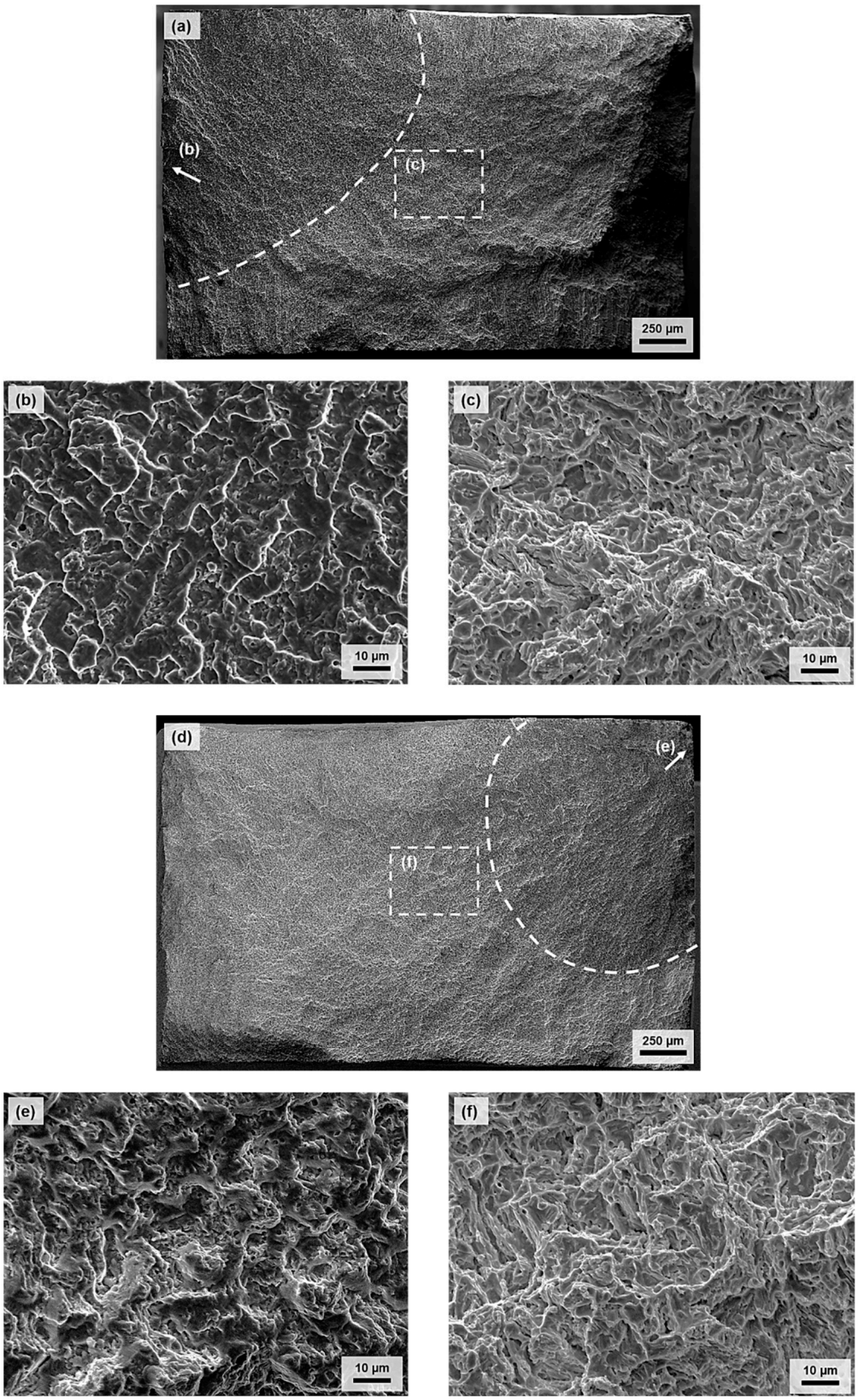


Figure 11. SEM micrographs of fracture surfaces after fatigue testing at a total strain amplitude of $\Delta\varepsilon_t/2 = \pm 0.5\%$ for the DED SS 316L in (**a**–**c**) as-built and (**d**–**f**) SMAT processed conditions. The subimages (**b**,**c**) and (**e**,**f**) show magnified views of the areas marked in (**a**,**d**) with a white arrow and white dashed rectangle, respectively.

4. Conclusions

In the present work, SS 316L was processed by DED and subsequently subjected to SMAT. Besides characterization of hardness and tensile tests, LCF tests with different strain amplitudes were performed focusing on both the as-built and SMAT processed conditions. Fracture surfaces and microstructure were thoroughly characterized by SEM and TEM. The effects of the SMAT processing on the microstructural and mechanical properties of 316L parts were finally evaluated. The following conclusions can be drawn from the results presented:

- The as-built DED microstructure consisted of large columnar grains nearly orientated along the building direction featuring a slight ⟨101⟩ texture. EBSD analysis revealed a small volume fraction of δ-ferrite at interdendritic and subgrain boundaries. TEM studies revealed the formation of dislocation cells promoted by rapid cooling rates and intrinsic heat treatment.
- As a result of the SMAT treatment, the formation of nanograins and nanotwins in the near-surface area was revealed by TEM. Moreover, results obtained by hardness mappings revealed that almost 50% of the cross-sections of surface treated specimens were strengthened by the SMAT process.
- Monotonic tensile loading revealed ductile material behavior of the DED SS 316L as-built condition, being characterized by YS, UTS and elongation at fracture of 300 MPa, 715 MPa and 19%, respectively. After SMAT treatment, the strength of the material was increased (YS and UTS of 375 and 800 MPa) due to the surface strengthening, alongside a concomitant loss of ductility (elongation at fracture of 6.5%).
- The cyclic deformation response of both as-built and SMAT conditions is characterized by slight cyclic softening. For the lowest total strain amplitude considered, fatigue properties of the DED SS 316L were improved as a result of the SMAT treatment. At higher strain amplitudes, the as-built condition was characterized by superior fatigue properties.
- Irrespective of the condition considered, post fatigue fractography revealed crack initiation solely in the direct vicinity of the side surfaces. Sub-surface crack initiation known from mechanical surface treatment processes could not be observed for the SMAT condition at the strain levels considered. Due to the surface treatment only being carried out on two large sides of the surface, the side surfaces represented the weakest link under cyclic loading. As a result, the conditions are characterized by similar crack initiation behavior. The increased brittleness of the SMAT condition therefore leads to an increased crack growth, eventually leading to inferior fatigue properties at high plastic strains.

Author Contributions: Conceptualization, T.W. (Thomas Wegener) and T.W. (Tao Wu); Methodology, T.W. (Thomas Wegener) and T.W. (Tao Wu); Investigation, T.W. (Thomas Wegener), T.W. (Tao Wu), F.S. and C.W.; Writing—Original Draft Preparation, T.W. (Thomas Wegener) and T.W. (Tao Wu); Writing—Review and Editing, T.W. (Thomas Wegener), T.W. (Tao Wu), J.L. and T.N.; Visualization, T.W. (Thomas Wegener) and T.W. (Tao Wu); Supervision, T.N. and J.L.; Project Administration, T.N. and J.L.; Funding Acquisition, T.N. and J.L. All authors have read and agreed to the published version of the manuscript.

Funding: Joint Research Group Program between Kassel University and Shenzhen Research Institute, City University of Hong Kong funded by Sino-German Center for Research Promotion (SGC) with project number GZ 1581. A part of this study was supported by the Ministry of Education, Culture, Sports, Science and Technology through a Grant-in-Aid for EarlyCareer Scientists 20K15057 (2020–2022).

Data Availability Statement: The data presented in this study are available upon request from the corresponding author.

Acknowledgments: The authors would like to thank Rolf Diederich and Rainer Hunke for technical support regarding the maintenance and operation of the laboratory equipment, and Marcel Krochmal for specimen preparation. Additionally, the authors appreciate Dewei Deng for providing stainless steel 316L specimens fabricated by direct energy deposition.

Conflicts of Interest: The authors declare no conflict of interest. The funding agency had no influence on the design of the study, the collection, analysis or interpretation of data, the writing of the manuscript; or the decision to publish the results.

References

1. Abdulhameed, O.; Al-Ahmari, A.; Ameen, W.; Mian, S.H. Additive manufacturing: Challenges, trends, and applications. *Adv. Mech. Eng.* **2019**, *11*, 168781401882288. [CrossRef]
2. Wegener, T.; Koopmann, J.; Richter, J.; Krooß, P.; Niendorf, T. CuCrZr processed by laser powder bed fusion—Processability and influence of heat treatment on electrical conductivity, microstructure and mechanical properties. *Fatigue Fract. Eng. Mat. Struct.* **2021**, *44*, 2570–2590. [CrossRef]
3. Zerbst, U.; Bruno, G.; Buffiere, J.-Y.; Wegener, T.; Niendorf, T.; Wu, T.; Zhang, X.; Kashaev, N.; Meneghetti, G.; Hrabe, N.; et al. Damage tolerant design of additively manufactured metallic components subjected to cyclic loading: State of the art and challenges. *Prog. Mater. Sci.* **2021**, *121*, 100786. [CrossRef] [PubMed]
4. Liverani, E.; Toschi, S.; Ceschini, L.; Fortunato, A. Effect of selective laser melting (SLM) process parameters on microstructure and mechanical properties of 316L austenitic stainless steel. *J. Mater. Process. Technol.* **2017**, *249*, 255–263. [CrossRef]
5. Wang, X.; Deng, D.; Yi, H.; Xu, H.; Yang, S.; Zhang, H. Influences of pulse laser parameters on properties of AISI316L stainless steel thin-walled part by laser material deposition. *Opt. Laser Technol.* **2017**, *92*, 5–14. [CrossRef]
6. Sibisi, P.N.; Popoola, A.P.I.; Arthur, N.K.K.; Pityana, S.L. Review on direct metal laser deposition manufacturing technology for the Ti-6Al-4V alloy. *Int. J. Adv. Manuf. Technol.* **2020**, *107*, 1163–1178. [CrossRef]
7. Guo, P.; Zou, B.; Huang, C.; Gao, H. Study on microstructure, mechanical properties and machinability of efficiently additive manufactured AISI 316L stainless steel by high-power direct laser deposition. *J. Mater. Process. Technol.* **2017**, *240*, 12–22. [CrossRef]
8. Zhang, K.; Wang, S.; Liu, W.; Shang, X. Characterization of stainless steel parts by Laser Metal Deposition Shaping. *Mater. Des.* **2014**, *55*, 104–119. [CrossRef]
9. Sun, G.F.; Shen, X.T.; Wang, Z.D.; Zhan, M.J.; Yao, S.; Zhou, R.; Ni, Z.H. Laser metal deposition as repair technology for 316L stainless steel: Influence of feeding powder compositions on microstructure and mechanical properties. *Opt. Laser Technol.* **2019**, *109*, 71–83. [CrossRef]
10. Syed, W.U.H.; Pinkerton, A.J.; Liu, Z.; Li, L. Coincident wire and powder deposition by laser to form compositionally graded material. *Surf. Coat. Technol.* **2007**, *201*, 7083–7091. [CrossRef]
11. AlHazaa, A.; Haneklaus, N. Diffusion Bonding and Transient Liquid Phase (TLP) Bonding of Type 304 and 316 Austenitic Stainless Steel—A Review of Similar and Dissimilar Material Joints. *Metals* **2020**, *10*, 613. [CrossRef]
12. Wang, X.; Deng, D.; Qi, M.; Zhang, H. Influences of deposition strategies and oblique angle on properties of AISI316L stainless steel oblique thin-walled part by direct laser fabrication. *Opt. Laser Technol.* **2016**, *80*, 138–144. [CrossRef]
13. Zheng, B.; Haley, J.C.; Yang, N.; Yee, J.; Terrassa, K.W.; Zhou, Y.; Lavernia, E.J.; Schoenung, J.M. On the evolution of microstructure and defect control in 316L SS components fabricated via directed energy deposition. *Mater. Sci. Eng. A* **2019**, *764*, 138243. [CrossRef]
14. Saboori, A.; Aversa, A.; Bosio, F.; Bassini, E.; Librera, E.; Chirico, M.; de Biamino, S.; Ugues, D.; Fino, P.; Lombardi, M. An investigation on the effect of powder recycling on the microstructure and mechanical properties of AISI 316L produced by Directed Energy Deposition. *Mater. Sci. Eng. A* **2019**, *766*, 138360. [CrossRef]
15. Thompson, S.M.; Bian, L.; Shamsaei, N.; Yadollahi, A. An overview of Direct Laser Deposition for additive manufacturing; Part I: Transport phenomena, modeling and diagnostics. *Addit. Manuf.* **2015**, *8*, 36–62. [CrossRef]
16. Shamsaei, N.; Yadollahi, A.; Bian, L.; Thompson, S.M. An overview of Direct Laser Deposition for additive manufacturing; Part II: Mechanical behavior, process parameter optimization and control. *Addit. Manuf.* **2015**, *8*, 12–35. [CrossRef]
17. Saboori, A.; Aversa, A.; Marchese, G.; Biamino, S.; Lombardi, M.; Fino, P. Microstructure and Mechanical Properties of AISI 316L Produced by Directed Energy Deposition-Based Additive Manufacturing: A Review. *Appl. Sci.* **2020**, *10*, 3310. [CrossRef]
18. Bedmar, J.; Riquelme, A.; Rodrigo, P.; Torres, B.; Rams, J. Comparison of Different Additive Manufacturing Methods for 316L Stainless Steel. *Materials* **2021**, *14*, 6504. [CrossRef]
19. DebRoy, T.; Wei, H.L.; Zuback, J.S.; Mukherjee, T.; Elmer, J.W.; Milewski, J.O.; Beese, A.M.; Wilson-Heid, A.; De, A.; Zhang, W. Additive manufacturing of metallic components–Process, structure and properties. *Prog. Mater. Sci.* **2018**, *92*, 112–224. [CrossRef]
20. Hunt, J.D. Steady state columnar and equiaxed growth of dendrites and eutectic. *Mater. Sci. Eng.* **1984**, *65*, 75–83. [CrossRef]
21. Morrow, B.M.; Lienert, T.J.; Knapp, C.M.; Sutton, J.O.; Brand, M.J.; Pacheco, R.M.; Livescu, V.; Carpenter, J.S.; Gray, G.T. Impact of Defects in Powder Feedstock Materials on Microstructure of 304L and 316L Stainless Steel Produced by Additive Manufacturing. *Met. Mat. Trans. A* **2018**, *49*, 3637–3650. [CrossRef]

22. Shin, W.-S.; Son, B.; Song, W.; Sohn, H.; Jang, H.; Kim, Y.-J.; Park, C. Heat treatment effect on the microstructure, mechanical properties, and wear behaviors of stainless steel 316L prepared via selective laser melting. *Mater. Sci. Eng. A* **2021**, *806*, 140805. [CrossRef]
23. Bagherifard, S.; Slawik, S.; Fernández-Pariente, I.; Pauly, C.; Mücklich, F.; Guagliano, M. Nanoscale surface modification of AISI 316L stainless steel by severe shot peening. *Mater. Des.* **2016**, *102*, 68–77. [CrossRef]
24. Olugbade, T.O.; Lu, J. Literature review on the mechanical properties of materials after surface mechanical attrition treatment (SMAT). *Nano Mater. Sci.* **2020**, *2*, 3–31. [CrossRef]
25. Roland, T.; Retraint, D.; Lu, K.; Lu, J. Fatigue life improvement through surface nanostructuring of stainless steel by means of surface mechanical attrition treatment. *Scr. Mater.* **2006**, *54*, 1949–1954. [CrossRef]
26. Huang, H.W.; Wang, Z.B.; Lu, J.; Lu, K. Fatigue behaviors of AISI 316L stainless steel with a gradient nanostructured surface layer. *Acta Mater.* **2015**, *87*, 150–160. [CrossRef]
27. Roland, T.; Retraint, D.; Lu, K.; Lu, J. Enhanced mechanical behavior of a nanocrystallised stainless steel and its thermal stability. *Mater. Sci. Eng. A* **2007**, *445–446*, 281–288. [CrossRef]
28. Maurel, P.; Weiss, L.; Bocher, P.; Grosdidier, T. Effects of SMAT at cryogenic and room temperatures on the kink band and martensite formations with associated fatigue resistance in a β-metastable titanium alloy. *Mater. Sci. Eng. A* **2021**, *803*, 140618. [CrossRef]
29. Shi, X.Y.; Liu, Y.; Li, D.J.; Chen, B.; Zeng, X.Q.; Lu, J.; Ding, W.J. Microstructure evolution and mechanical properties of an Mg–Gd alloy subjected to surface mechanical attrition treatment. *Mater. Sci. Eng. A* **2015**, *630*, 146–154. [CrossRef]
30. Yan, X.; Yin, S.; Chen, C.; Jenkins, R.; Lupoi, R.; Bolot, R.; Ma, W.; Kuang, M.; Liao, H.; Lu, J.; et al. Fatigue strength improvement of selective laser melted Ti6Al4V using ultrasonic surface mechanical attrition. *Mater. Res. Lett.* **2019**, *7*, 327–333. [CrossRef]
31. Sun, Y.; Bailey, R.; Moroz, A. Surface finish and properties enhancement of selective laser melted 316L stainless steel by surface mechanical attrition treatment. *Surf. Coat. Technol.* **2019**, *378*, 124993. [CrossRef]
32. Portella, Q.; Chemkhi, M.; Retraint, D. Influence of Surface Mechanical Attrition Treatment (SMAT) post-treatment on microstructural, mechanical and tensile behaviour of additive manufactured AISI 316L. *Mater. Charact.* **2020**, *167*, 110463. [CrossRef]
33. Belsvik, M.A.; Tucho, W.M.; Hansen, V. Microstructural studies of direct-laser-deposited stainless steel 316L-Si on 316L base material. *SN Appl. Sci.* **2020**, *2*, 1967. [CrossRef]
34. Andreau, O.; Koutiri, I.; Peyre, P.; Penot, J.-D.; Saintier, N.; Pessard, E.; Terris, T.; de Dupuy, C.; Baudin, T. Texture control of 316L parts by modulation of the melt pool morphology in selective laser melting. *J. Mater. Process. Technol.* **2019**, *264*, 21–31. [CrossRef]
35. Hsu, C.-H.; Chen, T.-C.; Huang, R.-T.; Tsay, L.-W. Stress Corrosion Cracking Susceptibility of 304L Substrate and 308L Weld Metal Exposed to a Salt Spray. *Materials* **2017**, *10*, 187. [CrossRef]
36. Tao, N.R.; Lu, J.; Lu, K. Surface Nanocrystallization by Surface Mechanical Attrition Treatment. *MSF* **2008**, *579*, 91–108. [CrossRef]
37. Pyun, Y.S.; Suh, C.M.; Yamaguchi, T.; Im, J.S.; Kim, J.H.; Amanov, A.; Park, J.H. Fatigue characteristics of SAE52100 steel via ultrasonic nanocrystal surface modification technology. *J. Nanosci. Nanotechnol.* **2012**, *12*, 6089–6095. [CrossRef]
38. Xie, J.; Zhu, Y.; Huang, Y.; Bai, C.; Ye, X. Microstructure Characteristics of 30CrMnSiNi2A Steel After Ultrasound-Aided Deep Rolling. *J. Mater. Eng. Perform.* **2013**, *22*, 1642–1648. [CrossRef]
39. Agrawal, A.K.; Singh, A.; Vivek, A.; Hansen, S.; Daehn, G. Extreme twinning and hardening of 316L from a scalable impact process. *Mater. Lett.* **2018**, *225*, 50–53. [CrossRef]
40. Wang, Z.D.; Sun, G.F.; Lu, Y.; Chen, M.Z.; Bi, K.D.; Ni, Z.H. Microstructural characterization and mechanical behavior of ultrasonic impact peened and laser shock peened AISI 316L stainless steel. *Surf. Coat. Technol.* **2020**, *385*, 125403. [CrossRef]
41. Jayalakshmi, M.; Huilgol, P.; Bhat, B.R.; Udaya Bhat, K. Insights into formation of gradient nanostructured (GNS) layer and deformation induced martensite in AISI 316 stainless steel subjected to severe shot peening. *Surf. Coat. Technol.* **2018**, *344*, 295–302. [CrossRef]
42. Bahl, S.; Suwas, S.; Ungàr, T.; Chatterjee, K. Elucidating microstructural evolution and strengthening mechanisms in nanocrystalline surface induced by surface mechanical attrition treatment of stainless steel. *Acta Mater.* **2017**, *122*, 138–151. [CrossRef]
43. Bertsch, K.M.; Meric de Bellefon, G.; Kuehl, B.; Thoma, D.J. Origin of dislocation structures in an additively manufactured austenitic stainless steel 316L. *Acta Mater.* **2020**, *199*, 19–33. [CrossRef]
44. Arifvianto, B.; Suyitno; Mahardika, M.; Dewo, P.; Iswanto, P.T.; Salim, U.A. Effect of surface mechanical attrition treatment (SMAT) on microhardness, surface roughness and wettability of AISI 316L. *Mater. Chem. Phys.* **2011**, *125*, 418–426. [CrossRef]
45. Naik, S.N.; Walley, S.M. The Hall–Petch and inverse Hall–Petch relations and the hardness of nanocrystalline metals. *J. Mater. Sci.* **2020**, *55*, 2661–2681. [CrossRef]
46. Oevermann, T.; Wegener, T.; Liehr, A.; Hübner, L.; Niendorf, T. Evolution of residual stress, microstructure and cyclic performance of the equiatomic high-entropy alloy CoCrFeMnNi after deep rolling. *Int. J. Fatigue* **2021**, *153*, 106513. [CrossRef]
47. Butz, A.; Zapara, M.; Helm, D. Modellierung von hochfesten und hochduktilen Blechwerkstoffen aus TWIP-Stahl. *wt Werkstattstech. Online* **2015**, *105*, 47–48. [CrossRef]
48. Yadollahi, A.; Shamsaei, N.; Thompson, S.M.; Seely, D.W. Effects of process time interval and heat treatment on the mechanical and microstructural properties of direct laser deposited 316L stainless steel. *Mater. Sci. Eng. A* **2015**, *644*, 171–183. [CrossRef]
49. Wang, Y.M.; Voisin, T.; McKeown, J.T.; Ye, J.; Calta, N.P.; Li, Z.; Zeng, Z.; Zhang, Y.; Chen, W.; Roehling, T.T.; et al. Additively manufactured hierarchical stainless steels with high strength and ductility. *Nat. Mater.* **2018**, *17*, 63–71. [CrossRef]

50. Saeidi, K.; Gao, X.; Zhong, Y.; Shen, Z.J. Hardened austenite steel with columnar sub-grain structure formed by laser melting. *Mater. Sci. Eng. A* **2015**, *625*, 221–229. [CrossRef]
51. Oevermann, T.; Wegener, T.; Niendorf, T. On the Evolution of Residual Stresses, Microstructure and Cyclic Performance of High-Manganese Austenitic TWIP-Steel after Deep Rolling. *Metals* **2019**, *9*, 825. [CrossRef]
52. Niendorf, T.; Lotze, C.; Canadinc, D.; Frehn, A.; Maier, H.J. The role of monotonic pre-deformation on the fatigue performance of a high-manganese austenitic TWIP steel. *Mater. Sci. Eng. A* **2009**, *499*, 518–524. [CrossRef]
53. Lambers, H.-G.; Rüsing, C.J.; Niendorf, T.; Geissler, D.; Freudenberger, J.; Maier, H.J. On the low-cycle fatigue response of pre-strained austenitic Fe61Mn24Ni6.5Cr8.5 alloy showing TWIP effect. *Int. J. Fatigue* **2012**, *40*, 51–60. [CrossRef]
54. Wegener, T.; Haase, C.; Liehr, A.; Niendorf, T. On the influence of κ-carbides on the low-cycle fatigue behavior of high-Mn light-weight steels. *Int. J. Fatigue* **2021**, *150*, 106327. [CrossRef]
55. Rajabi, E.; Miresmaeili, R.; Aliofkhazraei, M. The effect of surface mechanical attrition treatment (SMAT) on plastic deformation mechanisms and mechanical properties of austenitic stainless steel 316L. *Mater. Res. Express* **2019**, *6*, 1250g8. [CrossRef]
56. Schulze, V.; Hoffmeister, J. Mechanische Randschichtverfestigungsverfahren–Verfahren. In *Handbuch Wärmebehandeln und Beschichten*; Zoch, H.-W., Spur, G., Eds.; Carl Hanser Verlag GmbH & Co. KG: München, Germany, 2015; pp. 591–612. ISBN 978-3-446-42779-2.
57. Schulze, V. *Modern Mechanical Surface Treatment: States, Stability, Effects*; Wiley-VCH: Weinheim, Germany, 2006; ISBN 978-3-527-31371-6.
58. Tian, Y.Z.; Sun, S.J.; Lin, H.R.; Zhang, Z.F. Fatigue behavior of CoCrFeMnNi high-entropy alloy under fully reversed cyclic deformation. *J. Mater. Sci. Technol.* **2019**, *35*, 334–340. [CrossRef]
59. Manson, S.S.; Hirschberg, M.H. The role of ductility, tensile strength and fracture toughness in fatigue. *J. Frankl. Inst.* **1970**, *290*, 539–548. [CrossRef]
60. Mughrabi, H. Microstructural mechanisms of cyclic deformation, fatigue crack initiation and early crack growth. *Philos. Trans. A Math. Phys. Eng. Sci.* **2015**, *373*, 20140132. [CrossRef]
61. Xin, Q. Durability and reliability in diesel engine system design. In *Diesel Engine System Design*; Elsevier: Amsterdam, The Netherlands, 2013; pp. 113–202. ISBN 9781845697150.
62. Wegener, T.; Krochmal, M.; Oevermann, T.; Niendorf, T. Consequences of Deep Rolling at Elevated Temperature on Near-Surface and Fatigue Properties of High-Manganese TWIP Steel X40MnCrAl19-2. *Appl. Sci.* **2021**, *11*, 10406. [CrossRef]
63. Oguri, K. Fatigue life enhancement of aluminum alloy for aircraft by Fine Particle Shot Peening (FPSP). *J. Mater. Process. Technol.* **2011**, *211*, 1395–1399. [CrossRef]
64. Gao, T.; Sun, Z.; Xue, H.; Retraint, D. Effect of surface mechanical attrition treatment on high cycle and very high cycle fatigue of a 7075-T6 aluminium alloy. *Int. J. Fatigue* **2020**, *139*, 105798. [CrossRef]
65. Masing, G. Zur Heyn'schen Theorie der Verfestigung der Metalle durch verborgen elastische Spannungen. In *Wissenschaftliche Veröffentlichungen aus dem Siemens-Konzern*; Harries, C.D., Ed.; Springer: Berlin/Heidelberg, Germany, 1923; pp. 231–239. ISBN 978-3-642-98848-6.
66. Masing, G. Eigenspannungen in kaltgereckten Metallen. *Z. Für. Tech. Phys.* **1925**, *6*, 569–573.